Research Square

Preprints are preliminary reports that have not undergone peer review.
They should not be considered conclusive, used to inform clinical practice,
or referenced by the media as validated information.

Linking urban growth trajectories to surface urban heat island intensification in Indian cities

Cheolhee Yoo

cheolhee.yoo@pusan.ac.kr

Pusan National University https://orcid.org/0000-0002-3922-2300

Glynn Hulley

NASA Jet Propulsion Laboratory https://orcid.org/0000-0002-3266-179X

Ronita Bardhan

University of Cambridge https://orcid.org/0000-0001-5336-4084

Suniti Sanghavi

NASA Jet Propulsion Laboratory

Quentin Dehaene

New York University

ANAMIKA SHREEVASTAVA

New York University https://orcid.org/0000-0002-6805-7869

Article

Keywords:

Posted Date: November 20th, 2026

DOI: https://doi.org/10.21203/rs.3.rs-11664166/v1

License: This work is licensed under a Creative Commons Attribution 4.0 International License.
Read Full License

Additional Declarations: There is **NO** Competing Interest.

Linking urban growth trajectories to surface urban heat island intensification in Indian cities

Cheolhee Yoo[1,2,*], Glynn Hulley[1], Ronita Bardhan[3], Suniti Sanghavi[1], Quentin Dehaene[4], Anamika Shreevastava[4]

[1] Jet Propulsion Laboratory, California Institute of Technology, California, CA, USA
[2] Smart City Convergence Major, Pusan National University, Busan, South Korea
[3] Sustainable Design Group, University of Cambridge, Cambridge, UK
[4] New York University Tandon School of Engineering, Department of Mechanical and Aerospace Engineering, Brooklyn, NY, USA

* Corresponding author: Cheolhee Yoo (cheolhee.yoo@pusan.ac.kr)

ABSTRACT

Urban expansion and densification reshape cities in different ways, yet how they differ in their associations with long-term surface urban heat island change remains poorly understood across climatic settings. Here, we combine Local Climate Zone transitions with daily 375 m satellite land surface temperatures to assess warm-season daytime and nighttime surface urban heat island trends during 2013–2024 across five climatically diverse Indian cities. Densifying areas show stronger nighttime heat-island intensification than expanding areas in all five cities, with an overall difference of 0.52 K decade^{-1}. Daytime trends are lower in densifying than expanding areas in some cities, but higher in others. Sparsely built areas connect the two growth modes, serving as the leading destination of natural-land conversion and a major starting point of denser or taller built forms. Densification is relatively concentrated in inner zones, whereas expansion becomes more prevalent towards the periphery. Stronger nighttime intensification in densifying areas is also observed within two intermediate zones at comparable relative distances from city centers. These findings identify a consistent nighttime contrast between urban-growth pathways across diverse climatic settings and highlight the need to account for growth form and location in heat-resilient planning.

Introduction

The world is undergoing rapid urbanization, with global urban land area projected to nearly triple between 2000 and 2030[1]. By 2050, two-thirds of the world's population (68%) are projected to live in urban areas[2]. Urbanization modifies land cover and surface energy partitioning, contributing to the urban heat island (UHI) effect, in which urban areas are warmer than their non-urban surroundings[3,4]. The resulting urban warming can intensify residents' exposure to extreme heat, increase cooling energy demand and associated costs[5], and exacerbate heat-related health risks, including premature mortality[6].

These thermal effects depend in part on 'how' cities grow and 'where' that growth occurs. Urban areas often undergo multiple growth processes simultaneously, but these can broadly be classified into two main trajectories[7,8]: (i) horizontal expansion, which enlarges the urban footprint by converting previously non-urban surfaces, and (ii) densification, which intensifies development within existing urban areas through infill, increased building coverage and vertical growth. Examining the built forms that emerge through expansion and those that undergo densification can reveal structural connections between these growth trajectories. These trajectories alter local radiative exchange, heat storage, shading and ventilation in different ways[9,10], implying potentially divergent impacts on intra-urban heat patterns. The relative prevalence of expansion and densification can also change with distance from the urban center[11]. Characterizing how expansion and densification are distributed along the urban center–periphery gradient, and whether this ordering is consistent across cities, provides a spatial context for interpreting their thermal contrasts[12].

Two widely studied forms of UHI are canopy-layer UHI (CUHI), based on near-surface air temperature, and surface UHI (SUHI), based on land surface temperature (LST). Here, we focus on SUHI to examine how urban–non-urban surface temperature contrasts vary with changes in land cover and urban morphology. Although horizontal expansion has repeatedly been linked to increasing SUHI intensity[13,14], the thermal consequences of densification remain less well understood. This uncertainty is particularly important at night, when urban heat storage and geometry influence the release of stored energy and

the rate of nocturnal cooling[15]. Greater building density and volume can increase the amount of heat-storing urban material, while reduced sky-view factors restrict longwave radiative loss. Together, these morphological changes can delay nocturnal cooling even when taller buildings enhance daytime shading[10,16–19]. Recent evidence further suggests that vertically oriented urban renewal may reduce daytime LST while increasing nighttime LST[8]. These findings highlight the thermal effects of changes within existing urban areas, but do not explain how their long-term SUHI trends compare with those associated with outward expansion. Whether densification and expansion show consistent differences in daytime and nighttime SUHI trends across climatic settings therefore remains unclear.

India provides a particularly informative setting for addressing these questions. Its metropolitan regions exhibit varying combinations of horizontal expansion and densification, including vertical development[20,21]. These growth processes occur across climates ranging from semi-arid to tropical monsoon conditions[22]. Comparing cities across this climatic range provides an opportunity to examine whether the spatial organization of growth and its associated daytime and nighttime SUHI trends are shared across different environmental settings. Urbanization has already contributed substantially to nighttime surface warming in Indian cities[23], underscoring the relevance of distinguishing the thermal implications of different growth pathways. Such comparisons may also offer insights into other rapidly urbanizing cities in the Global South undergoing similar combinations of expansion and densification.

Two observational challenges have limited such comparisons. First, binary urban–non-urban maps capture horizontal expansion but provide limited information on structural changes associated with densification[24,25]. The Local Climate Zone (LCZ) framework distinguishes urban forms through building height, density and surface cover[26], yet producing comparable maps across years remains challenging in heterogeneous, rapidly changing cities, including those in India[27,28]. Second, trade-offs between spatial detail and temporal coverage in satellite thermal observations constrain long-term assessments of neighborhood-scale daytime and nighttime SUHI[29]. LST observations from the Visible

Infrared Imaging Radiometer Suite (VIIRS) at 375 m help address this observational gap by combining moderate spatial resolution with regular daytime and nighttime sampling[29,30].

Here, we integrate LCZ maps for 2013 and 2024 with 375-m VIIRS LST observations from 2013–2024 to examine the spatial organization and thermal changes associated with urban expansion and densification in five Indian cities: Delhi, Lucknow, Pune, Kolkata and Kochi. Using an LCZ-based urban-trajectory framework (Fig. 1), we identify built forms that serve both as destinations of natural-land conversion and as starting points for transitions to denser or taller development. We then examine how the relative prevalence of expansion and densification varies from the urban center towards the periphery and whether this pattern is shared across cities. We compare their warm-season daytime and nighttime SUHI trends both citywide and within zones at comparable relative distances from each city's center. Together, these analyses assess the extent to which urban growth patterns and associated thermal responses are shared across cities, providing comparative evidence to inform planning in both expanding urban margins and densifying urban areas.

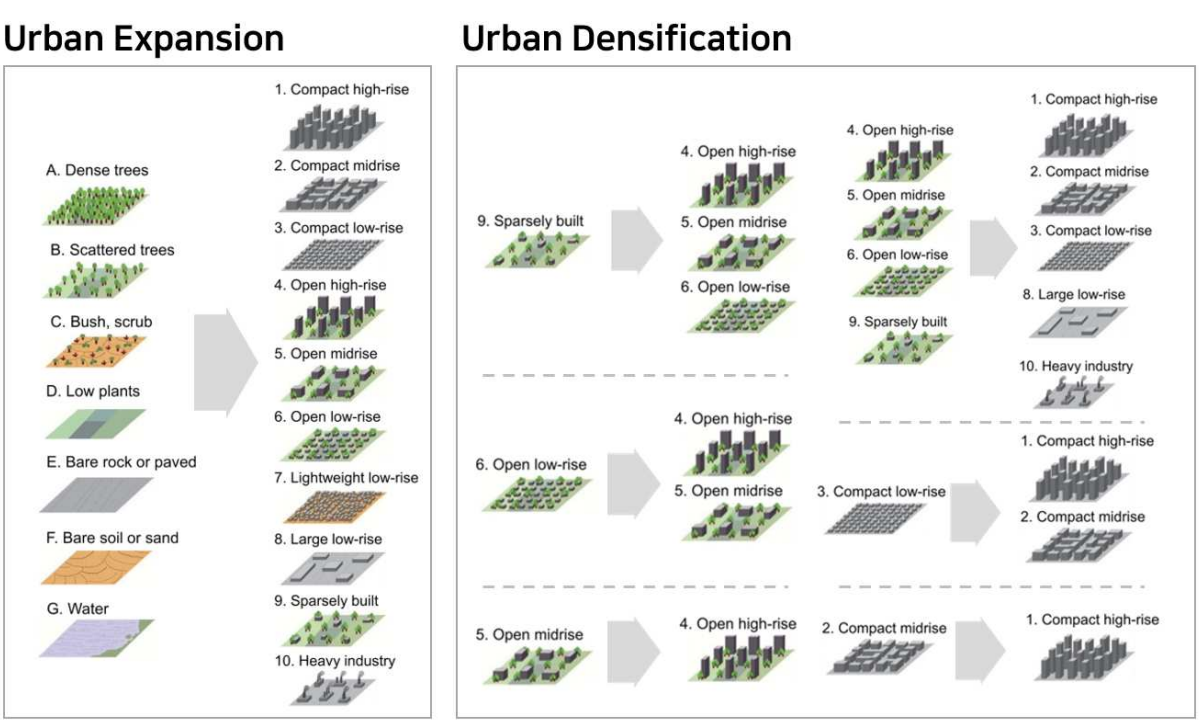


Fig. 1 | LCZ-based definitions of urban expansion and densification. Conceptual schematic illustrating urban growth trajectories defined from Local Climate Zone (LCZ) transitions. Urban expansion (left) comprises transitions from land-cover LCZs (A–G) to built LCZs (1–10). Urban densification (right) comprises selected transitions among built LCZs, including horizontal infill and vertical development towards denser or taller urban forms. Arrows indicate the transition pathways assigned to each growth trajectory in this study.

Results

Sparsely built areas link urban expansion and densification

We mapped LCZs across the five Indian cities for 2013 and 2024 (Fig. 2). Overall classification accuracy ranged from 90.3% to 97.1% for 2013 and from 94.4% to 97.1% for 2024 under a hybrid spatial validation procedure (Methods and Supplementary Figs. 1–5). We find that sparsely built areas (LCZ 9) constituted the largest built class in both 2013 and 2024, while low plants (LCZ D) were the most extensive non-water natural class across all five cities. LCZ transitions revealed a shared pattern of urban expansion, with sparsely built areas forming the principal destination of natural-land conversion (Fig. 2 and Supplementary Tab 1). Transitions from natural LCZs, primarily low plants, dense trees and bare soil, to LCZ 9 accounted for 46% of all pixels that changed LCZ class in Lucknow, 41% in both Kochi and Pune, 36% in Kolkata and 30% in Delhi. Although the share of this pathway varied among cities, its prominence across all five cities indicates that urban expansion most often resulted in sparsely built urban fabric.

Sparsely built areas also served as a major starting point for densification within existing urban land. Conversion from LCZ 9 to open low-rise areas (LCZ 6) accounted for 19% of all changed pixels in Delhi, 23% in Lucknow, 19% in Kolkata and 25% in Kochi (Fig. 2 and Supplementary Tab 1). Densification was also marked by the emergence of taller built forms. Open high-rise areas (LCZ 4) increased from 0.8% to 5.6% of the total mapped area in Pune and from 0.1% to 1.4% in Delhi, and were mapped in Lucknow and Kolkata in 2024 but not in 2013. Most of the newly mapped open high-rise area had been classified as sparsely built in 2013. Together, these transitions reveal a dual role for sparsely built areas in urban growth: they were both the leading destination of natural-land conversion and a major source of denser or taller urban development.

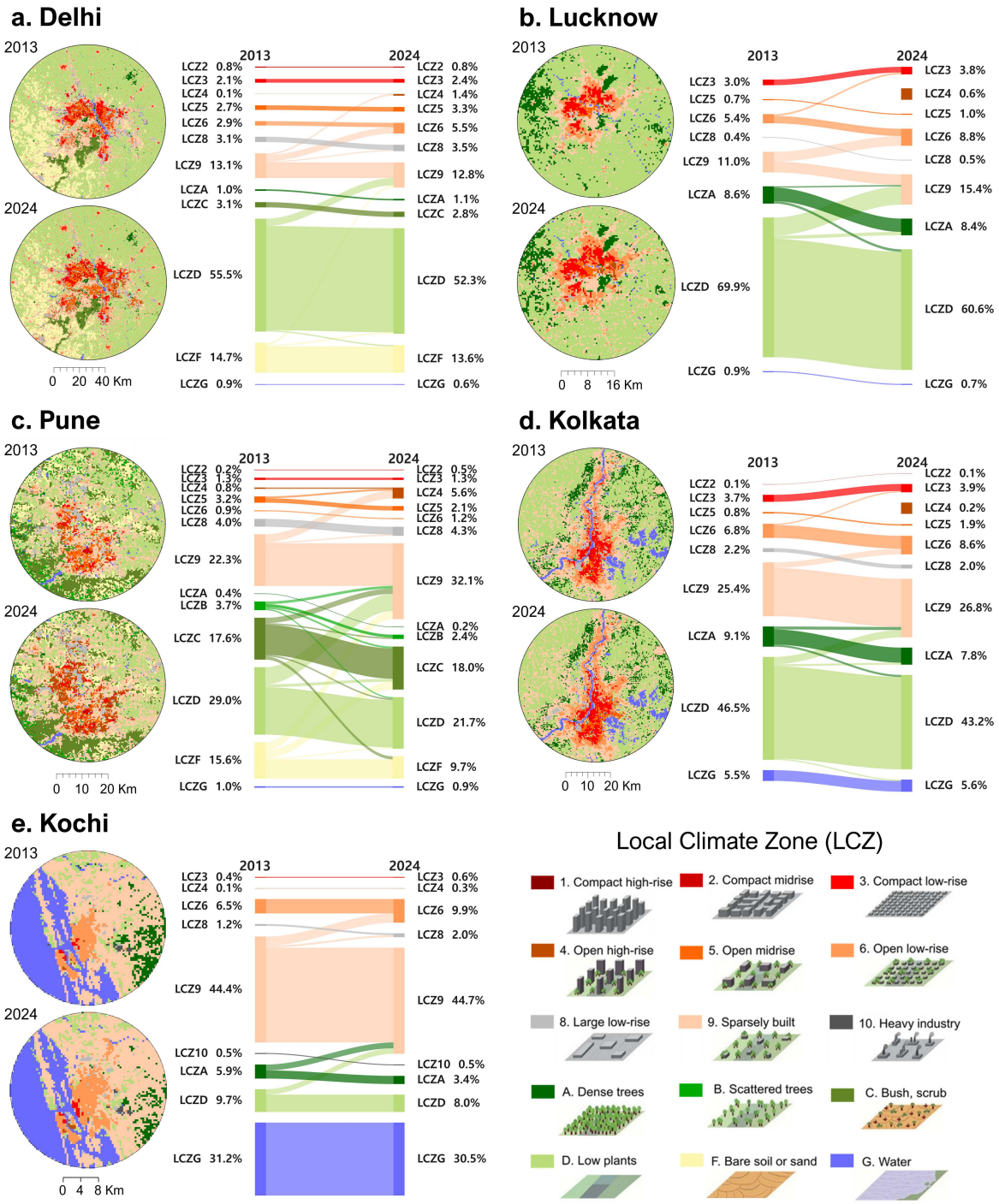


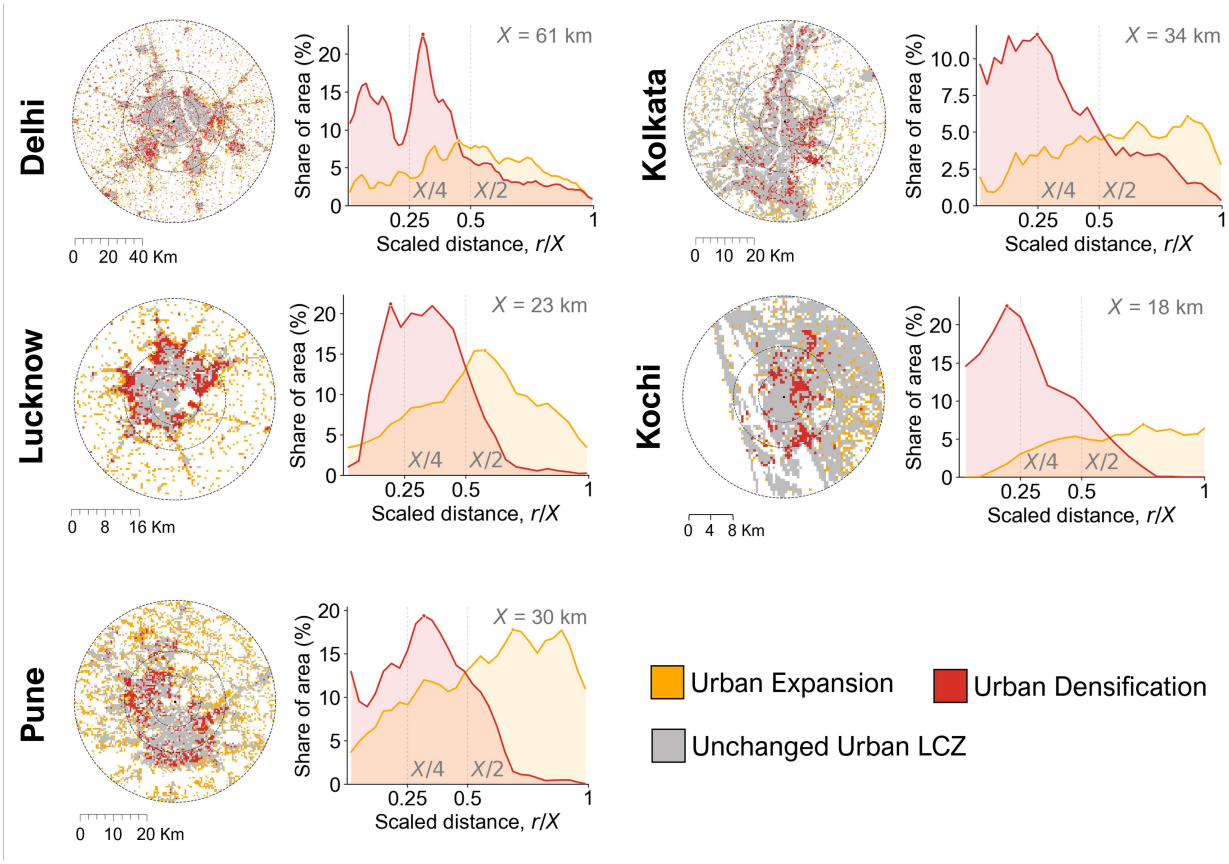
Fig. 2 | Spatial patterns and transitions of Local Climate Zones across five Indian cities, 2013–2024. a–e, Local Climate Zone (LCZ) maps and corresponding Sankey diagrams for Delhi, Lucknow, Pune, Kolkata and Kochi, respectively. In each panel, maps on the left show LCZ distributions in 2013 (top) and 2024 (bottom), while the Sankey diagram on the right illustrates LCZ transitions between the two years.

Flow widths are proportional to the area undergoing each transition, and percentages indicate the share of each LCZ class in the total mapped area in the respective year. Colors identify LCZ classes consistently across the maps and diagrams, as shown in the legend. The five largest transition pathways for each city are summarized in Supplementary Tab 1.

Urban expansion and densification follow a shared radial ordering

We next examined the spatial organization of urban expansion and densification. LCZ transitions were grouped into urban expansion, urban densification and unchanged urban LCZs following the classification scheme in Fig. 1. To compare cities of different sizes, radial distance from the urban centroid (r) was normalized by the city-specific maximum radius (X), which ranged from 18 km in Kochi to 61 km in Delhi. Across all five cities, urban expansion and densification exhibited a consistent radial ordering (Fig. 3). Densification generally accounted for a larger share of area than expansion in inner radial zones, whereas expansion became more prevalent farther from the centroid and typically exceeded densification near or beyond the middle of the radial extent. This spatial pattern was particularly clear in Lucknow, Pune and Kochi. In Delhi and Kolkata, the two growth modes showed more comparable area shares across intermediate radial zones, indicating a weaker radial separation. The same overall ordering was evident in the absolute radial area profiles (Supplementary Fig. 6).

The relative extent of the two growth modes nevertheless differed substantially among cities (Supplementary Fig. 7). Expansion covered approximately 2.6 times as much area as densification in Pune (260 versus 100 km²) and 1.6 times as much in Lucknow (115 versus 74 km²). In contrast, densification covered more area than expansion in Delhi, at approximately 440 and 330 km², respectively. The two modes occupied similar total areas in Kolkata (approximately 100 km² each), while expansion moderately exceeded densification in Kochi (40 versus 30 km²). Thus, the balance between expansion and densification varied among cities, but their relative concentration towards the periphery and the center, respectively, remained consistent.



166

167 **Fig. 3 | Spatial distribution and radial organization of urban-growth trajectories between 2013 and**
168 **2024.** a–e, Urban-growth trajectories were derived from Local Climate Zone (LCZ) transitions following the
169 classification scheme in Fig. 1. Maps show urban expansion (orange), urban densification (red) and
170 unchanged urban LCZs (grey) in Delhi, Lucknow, Pune, Kolkata and Kochi. White areas indicate locations
171 not assigned to any of the three displayed urban-growth categories. Adjacent curves show the area
172 occupied by expansion (orange) or densification (red) in each radial zone, divided by the total area of that
173 zone and expressed as a percentage. Profiles show these within-zone shares smoothed with a centered
174 three-annulus moving average; the area under either curve is not normalized to 100%. Radial distance from
175 the urban centroid (r) is normalized by the city-specific maximum radius (X), whose value is indicated in
176 each plot. Vertical dashed lines mark r/X = 0.25 and 0.5.

177 **Daytime and nighttime SUHI trends exhibit contrasting radial patterns**

178 We compared daytime and nighttime SUHI trends across radial zones. SUHI intensity
179 was calculated as the difference between local LST and the citywide mean LST of pixels
180 that retained the same natural LCZ class (A–F, excluding water) in both years (Methods).
181 In 2013 and 2024, compact and open built LCZs generally exhibited higher nighttime

SUHI intensity than sparsely built areas, whereas daytime contrasts among LCZs varied across cities (Supplementary Figs. 8 and 9). We examined how SUHI trends varied between day and night and across radial zones, estimating trends for March–June 2013–2024 using RemotePARTS (Methods). Mean nighttime SUHI trends were positive in all five cities, ranging from 0.1 K decade^{-1} in Kochi to 0.7 K decade^{-1} in Lucknow (Fig. 4). Delhi and Pune each showed mean trends of 0.4 K decade^{-1}, while Kolkata reached 0.3 K decade^{-1}. In contrast, daytime trends differed in both sign and magnitude: mean trends were slightly negative in Delhi (−0.2 K decade^{-1}), Lucknow and Pune (−0.1 K decade^{-1} each), but positive in Kolkata (0.8 K decade^{-1}) and Kochi (0.2 K decade^{-1}). Spatial standard deviations of trends were consistently greater during the day (0.8–1.3 K decade^{-1}) than at night (0.4–0.6 K decade^{-1}), indicating stronger daytime heterogeneity within cities.

Nighttime radial profiles showed that the positive citywide means were accompanied by substantial spatial variation (Fig. 4). Delhi, Lucknow and Pune exhibited broad hump-shaped profiles, with trends strengthening from the centroid towards inner-to-intermediate radial zones before declining towards the periphery. This pattern was most distinct in Lucknow, where the radial mean exceeded 1 K decade^{-1} near $r/X \approx 0.4$. Delhi additionally showed a reversal from negative trends near the centroid to positive trends in intermediate radial zones. Kolkata exhibited a more gradual outward decline, whereas Kochi showed weaker, non-monotonic radial variation.

Daytime profiles followed a contrasting pattern, with trends generally shifting towards more positive values at greater radial distances in Delhi, Lucknow, and Pune (Fig. 4). In Delhi and Pune, negative trends in inner zones gave way to positive trends beyond the middle radial zone. Lucknow followed a similar but weaker pattern, with near-zero to weakly positive trends in outer zones. Kochi showed a non-monotonic profile: strongly positive trends near the centroid became negative at inner-to-intermediate radii before returning to modestly positive values farther out. Kolkata maintained positive daytime trends across its entire radial extent, with relatively modest radial variation.

The negative or near-zero daytime means in Delhi, Lucknow and Pune therefore combined inner-zone SUHI weakening with outer-zone intensification. Citywide averages concealed opposing changes within individual cities, while radial profiles revealed distinct spatial patterns between day and night. These patterns provide context for comparing SUHI trends between urban expansion and densification.

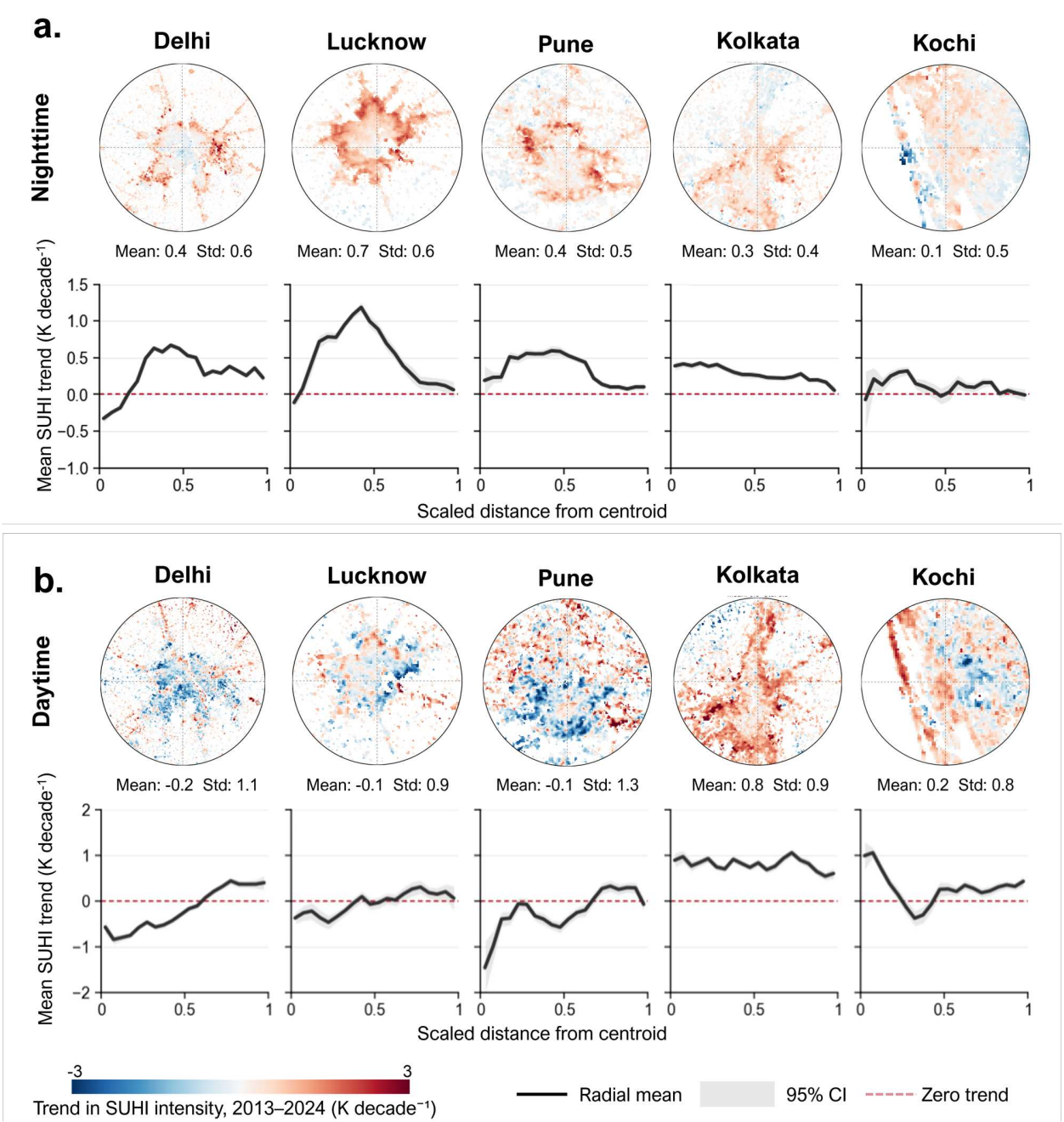


Fig. 4 | Spatial and radial trends in daytime and nighttime surface urban heat-island intensity across the five study cities. Pixel-level trends in surface urban heat-island (SUHI) intensity were estimated for March–June 2013–2024 using remotePARTS autoregressive models with an AR(1) error structure and are expressed in K decade^{-1}. The upper two rows show nighttime trends and the lower two rows show daytime trends. Circular maps display pixel-level estimates. Annotations beneath each map report the spatial mean and sample standard deviation across valid pixels assigned to urban expansion, urban densification or unchanged urban LCZs. Radial profiles use the same boundary-derived centroid and city-specific maximum radius (X) as Fig. 3, applied consistently to daytime and nighttime. Distance from the centroid (r) was normalized by X, and pixels within r/X ≤ 1 were grouped into 20 equal-width bins of 0.05. Mean trends were calculated for bins containing at least five valid pixels. Black lines connect bin means at their midpoints without additional smoothing. Grey shading denotes approximate 95% confidence intervals, calculated as mean ± 1.96s/√n, where s is the within-bin sample standard deviation and n is the number of valid pixels. These intervals do not account for spatial autocorrelation or uncertainty in individual trend estimates. Red dashed lines mark zero trend. Maps and radial profiles include all valid trend estimates within the three trajectories, irrespective of statistical significance; other categories and missing values are excluded. Circular outlines indicate the reference circles of radius X.

Densification shows stronger nighttime SUHI intensification than expansion

We compared SUHI trend distributions across three urban-growth trajectories: urban expansion, urban densification and unchanged urban LCZs (Fig. 5). Densification exhibited the highest median nighttime SUHI trend among the three trajectories in all five cities (Fig. 5a). The densification–expansion difference in median trends was largest in Lucknow (+0.87 K decade^{-1}), followed by Pune (+0.68), Kochi (+0.50), Kolkata (+0.38) and Delhi (+0.22 K decade^{-1}). Unchanged urban LCZs generally occupied an intermediate position, although their nighttime trends did not differ significantly from those of expansion in Delhi. The pooled cross-city difference between densification and expansion was +0.52 K decade^{-1} (95% CI, +0.21 to +0.84; Fig. 5c), consistent with the higher nighttime SUHI trends in densifying areas observed in each city.

Daytime differences between densification and expansion varied across cities (Fig. 5b,d). Densification had lower median SUHI trends than expansion in Delhi (−0.12 K decade^{-1}), Lucknow (−0.23 K decade^{-1}) and Pune (−0.93 K decade^{-1}), whereas higher median trends were observed in Kolkata (+0.68 K decade^{-1}) and Kochi (+0.60 K

decade⁻¹). Spatial block bootstrap 95% confidence intervals for these median differences excluded zero in Pune, Kolkata and Kochi but included zero in Delhi and Lucknow (Fig. 5d). The pooled daytime difference was close to zero (+0.01 K decade⁻¹; 95% CI, −0.81 to +0.83), reflecting oppositely signed city-specific estimates. Restricting the natural reference to low plants (LCZ D) preserved the signs of the city-specific point estimates: nighttime differences remained positive in all five cities, while daytime differences remained negative in Delhi, Lucknow and Pune and positive in Kolkata and Kochi (Supplementary Fig. 10).

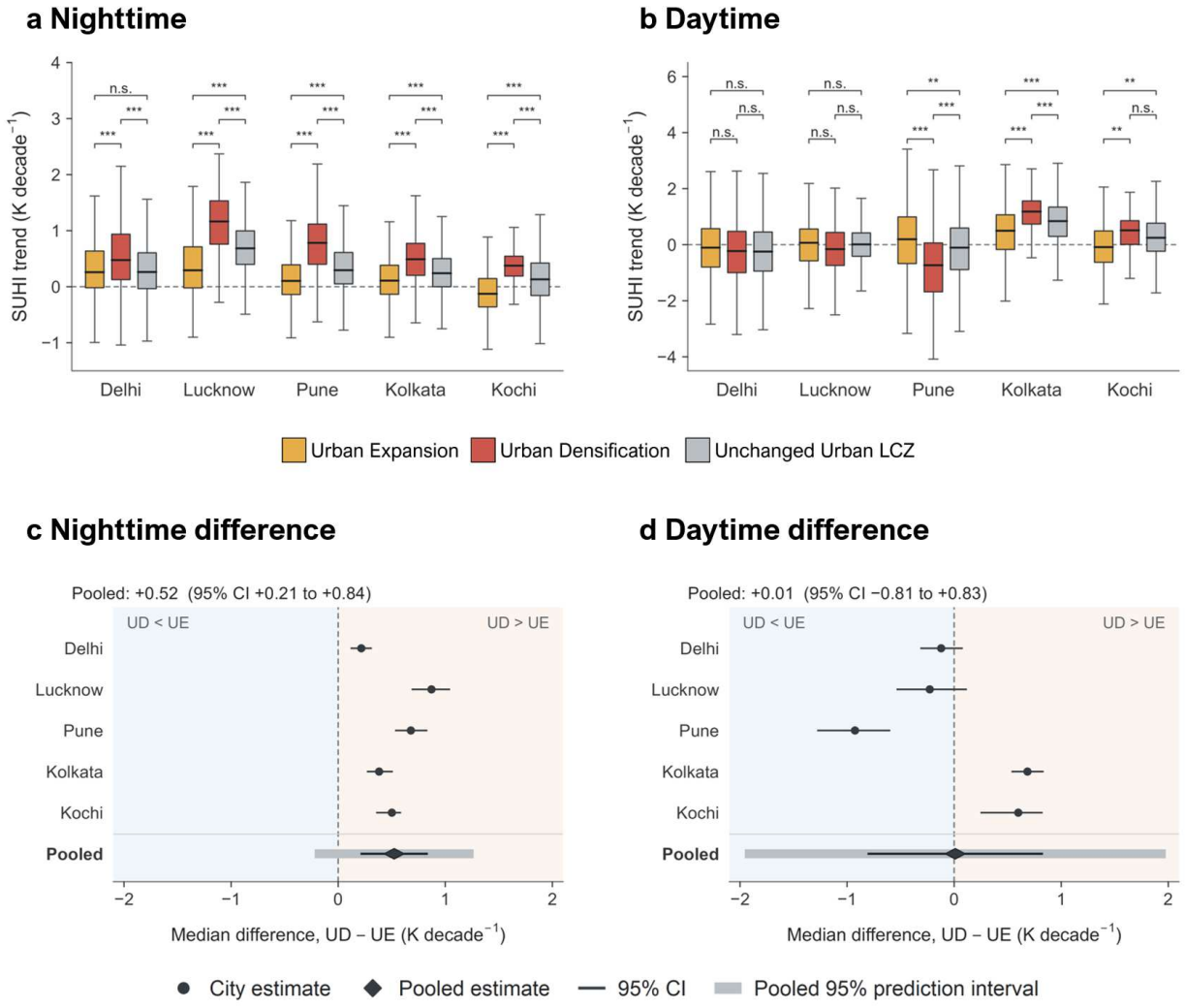


Fig. 5 | Nighttime and daytime SUHI trends across urban-growth trajectories. a,b, Pixel-level distributions of nighttime (a) and daytime (b) trends in surface urban heat-island (SUHI) intensity for urban

expansion (UE; orange), urban densification (UD; red) and unchanged urban Local Climate Zones (LCZs; grey) in Delhi, Lucknow, Pune, Kolkata and Kochi. Trends were estimated from March–June observations during 2013–2024. Boxes span the 25th–75th percentiles, central lines indicate medians, and whiskers extend to the most extreme observations within 1.5 times the interquartile range below the first quartile or above the third quartile. Outlier points are not displayed but are retained in all calculations. Brackets indicate pairwise comparisons of median trends using approximate two-sided, null-centred spatial block bootstrap tests with 10,000 replicates. Blocks were resampled independently within each trajectory. P values were Holm-adjusted across the three pairwise comparisons within each city and observation period: *P < 0.05, **P < 0.01 and ***P < 0.001; n.s., P ≥ 0.05. **c,d,** Differences in median SUHI trends between densification and expansion (UD − UE) for nighttime (c) and daytime (d). Circles indicate city-specific estimates, with horizontal black lines showing unadjusted 95% percentile confidence intervals (CIs) derived from 10,000 trajectory-stratified spatial block bootstrap replicates. Diamonds indicate pooled random-effects estimates across the five cities; black lines show pooled 95% CIs, and thick grey bars show 95% prediction intervals. Between-city variance was estimated by restricted maximum likelihood, and pooled CIs were calculated using Hartung–Knapp inference. Light blue and orange shading indicate negative (UD < UE) and positive (UD > UE) contrasts, respectively. Grey dashed lines mark zero trend in a,b and zero contrast in c,d. All trends and contrasts are expressed in K decade^{-1}.

Comparisons within the same radial zones revealed higher nighttime SUHI trends in densifying areas at intermediate distances and more city-specific daytime differences (Supplementary Fig. 11). Nighttime differences in median SUHI trends between densification and expansion were positive in all five cities within the two zones spanning r/X = 0.5–0.7, ranging from +0.14 to +0.73 K decade^{-1}. Confidence intervals were unavailable for some of these differences, including both zones in Kochi. This nighttime ordering varied locally, with Delhi showing lower nighttime SUHI trends in densifying than in expanding areas in its two innermost zones (r/X < 0.2). During the day, differences in median trends were consistently negative in Pune and positive in Kolkata and Kochi across radial zones with sufficient samples. Delhi showed differences of both signs, whereas daytime confidence intervals in Lucknow included zero wherever they could be estimated.

SUHI measures the surface temperature difference between urban and natural areas, so an increasing SUHI does not necessarily indicate absolute urban warming. At night, LST generally declined in expansion, densification, unchanged urban and natural

reference areas (Supplementary Fig. 12). The decline was often smaller in densifying areas than in the natural reference, producing a positive SUHI trend. Densifying areas also showed smaller LST declines than expanding areas, particularly in Lucknow and Pune. During the day, densifying areas in Pune showed decreases in both LST and SUHI. In Kolkata, LST declined but SUHI increased because the natural reference cooled more. In Kochi, both LST and SUHI increased. Thus, increasing SUHI can reflect either absolute surface warming or a smaller temperature decline than in the natural reference.

We further examined individual LCZ transition pathways that accounted for at least 10% of pixels within the expansion or densification group in each city (Supplementary Figs. 13 and 14). Among the pathways meeting this threshold, transitions from sparsely built to open high-rise areas (LCZ 9→4) showed stronger nighttime SUHI increases than transitions from sparsely built to open low-rise areas (LCZ 9→6) in Delhi and from open mid-rise to open high-rise areas (LCZ 5→4) in Pune. Expansion trends also differed by initial land cover: conversion from low plants to sparsely built areas (LCZ D→9) generally showed stronger nighttime increases than conversion from bare soil (LCZ F→9) or bush and scrub (LCZ C→9). During the day, transitions from sparsely built to open high-rise areas showed the most negative trends among the selected pathways in Delhi and Pune. Densification pathways in Kolkata and Kochi showed positive daytime trends, particularly transitions from sparsely built to open low-rise areas. These results show that densification was associated with higher nighttime SUHI trends, whereas daytime trends varied by LCZ transition and city.

Discussion

Across the five Indian cities, densification was concentrated in inner urban zones, whereas expansion became increasingly prevalent towards the periphery. Despite differences in the relative extent of these growth modes, densifying areas showed higher nighttime SUHI trends than expanding areas in every city. Daytime differences were less consistent: densifying areas had lower SUHI trends than expanding areas in Delhi, Lucknow and Pune, but higher trends in Kolkata and Kochi. By linking LCZ transitions

between 2013 and 2024 with multi-year SUHI trends, our analysis distinguishes thermal changes accompanying outward expansion from those associated with the transformation of existing built areas. This trajectory-based perspective complements studies of urban expansion and static urban-form contrasts[8,31–36]. Understanding long-term urban thermal change therefore requires distinguishing both the form of development and the time of observation.

The greater prevalence of densification in inner zones is consistent with infill and redevelopment within existing urban areas, whereas the outward increase in expansion reflects conversion of natural land near the urban margins. Natural-land conversion most often produced sparsely built areas, while many areas that were sparsely built in 2013 became denser or taller built forms by 2024. Distinguishing these transitions reveals changes that are obscured when all built land is grouped into a single category. Expansion and densification nevertheless occurred within overlapping radial zones, particularly in Delhi and Kolkata. The shared center–periphery pattern therefore describes where each growth mode was more prevalent, rather than a separation into exclusively expanding and densifying zones.

The nighttime association is consistent with the influence of building mass and urban geometry on heat storage and radiative exchange. Additional building mass can increase heat storage, while reduced sky exposure can restrict radiative heat loss from street-level surfaces after sunset[17,37–39]. These mechanisms could help explain why densification exhibited stronger nighttime SUHI intensification than the predominantly sparse forms associated with expansion. Densifying areas also had higher nighttime SUHI trends than expanding areas within the two adjacent radial zones spanning r/X = 0.5–0.7 in all five cities (Supplementary Fig. 11a). This indicates that the citywide pattern was also present at comparable relative distances from the urban center, although confidence intervals could not be estimated for all city–zone comparisons.

The greater variation in daytime differences between densification and expansion suggests a stronger role for the specific urban-form transition and its environmental setting. Shading, solar exposure, albedo and moisture availability can exert competing

influences on daytime surface temperature[40–43]. In Delhi and Pune, areas that transitioned from sparsely built to open high-rise forms exhibited decreasing daytime SUHI alongside nighttime SUHI intensification (Supplementary Figs. 13 and 14). Increased shading is one possible explanation for this contrast[18], although these transitions also encompass changes in building coverage, vegetation and surface materials. Positive daytime trends along densification pathways in Kolkata and Kochi, both of which have humid climates, point to a different balance of influences. Where vegetation has adequate access to water, evaporative cooling of natural surfaces could strengthen their surface temperature difference from built surfaces[44]. Measurements of changes in soil moisture, vegetation and surface energy exchange would be needed to determine whether this mechanism explains the differences among cities.

Interpreting these SUHI trends also requires separating changes in relative SUHI intensity from changes in absolute LST. Positive nighttime SUHI trends often occurred alongside declining nighttime LST, reflecting a smaller long-term decline in densifying areas than in the natural reference. This finding describes how surface temperatures changed across years; it does not measure the rate of cooling within an individual night. The daytime trends in densifying areas in Kolkata and Kochi illustrate the same distinction: SUHI intensified while absolute LST declined in Kolkata, whereas both increased in Kochi (Fig. 5b and Supplementary Fig. 12b). Thus, similar changes in SUHI can accompany different absolute temperature trajectories. Reporting both quantities helps distinguish a strengthening urban–natural thermal contrast from absolute surface warming and makes clear what the observed trends can support about urban thermal change.

These findings support evaluating urban expansion and densification separately in urban thermal assessments. The consistently higher nighttime SUHI trends in densifying areas highlight the importance of including nighttime observations when assessing the thermal changes associated with densification. Daytime assessments should account for the specific development pathways and local environmental setting, given the opposing densification–expansion differences among cities. Reporting SUHI alongside absolute

LST trends would further help planners distinguish changes in the urban–natural temperature contrast from absolute surface warming or cooling.

Several limitations constrain the interpretation of these associations. Errors in the two LCZ maps can propagate into transition assignments. Areas that retain the same LCZ classification may still undergo physical changes. The endpoint maps identify net change but cannot establish construction dates or intermediate transitions, including whether individual locations passed sequentially from natural land through sparsely built to denser forms.

VIIRS measures clear-sky radiometric surface temperature, and viewing geometry and thermal anisotropy can affect its representation of complex urban surfaces. The observed SUHI trends do not directly quantify changes in near-surface air temperature or human heat exposure. Combining repeated observations of urban structure and meteorological conditions with surface energy-balance measurements and process-based modelling would allow the proposed mechanisms to be evaluated more directly and across a wider range of conditions. Complementary air-temperature and exposure data would help determine how the observed surface-temperature changes relate to human heat exposure and adaptation needs. Within these limits, the five-city comparison shows consistently higher nighttime SUHI trends in densifying than in expanding areas, whereas daytime differences vary among cities. These findings connect the spatial organization of urban growth with its thermal evolution and demonstrate why changes in urban–natural temperature contrasts need to be interpreted alongside absolute surface temperature trends.

Materials and Methods

Study regions and analysis boundaries

We examined urban growth and SUHI change in Delhi, Lucknow, Pune, Kolkata and Kochi, spanning contrasting climatic settings and urban development trajectories in India (Supplementary Fig. 15). Delhi represents a predominantly semi-arid setting, Lucknow the humid subtropical Gangetic Plain, Pune the transition between tropical wet–dry and

hot semi-arid climates, Kolkata a tropical wet–dry setting influenced by the Bay of Bengal, and Kochi a tropical monsoon climate[22]. This climatic range allowed the relationship between urban growth and SUHI change to be examined across different thermal and moisture environments.

Background climate was characterized using India Meteorological Department station normals for 1991–2020[45]. For consistency with the thermal analysis, mean air temperature was averaged over March–June warm-season period, and relative humidity was averaged from the corresponding monthly observations at 17:30 Indian Standard Time. Mean temperature and afternoon relative humidity were approximately 29.4°C and 33% in Delhi, 29.6°C and 36% in Lucknow, 28.1°C and 37% in Pune, 30.2°C and 64% in Kolkata, and 28.7°C and 70% in Kochi.

Urban extents were delineated using the Global Hierarchical Urban Boundaries dataset (GHUB)[46]. Each boundary was expanded outward by 5 km to include surrounding natural areas for the SUHI reference. This buffer width is consistent with previous urban thermal studies using 5-km extensions of urban analysis domains or surrounding non-urban reference zones[47,48]. These buffered polygons defined the baseline study regions and the reference geometry for radial analyses.

LCZ mapping

Reference samples and predictor data

LCZ maps were produced for 2013 and 2024 using a consistent classification framework. For each city, reference sampling covered an expanded rectangular domain defined using a 25 km buffer to improve the representation of natural land-cover classes (LCZ A–G) in the surrounding landscape. This reference-sampling domain extended beyond the 5 km-buffered study footprint used for subsequent urban-growth and thermal analyses.

Within each sampling domain, reference polygons representing spatially homogeneous LCZ units were manually delineated for each city and target year, following the WUDAPT framework[49]. Predictor values were extracted for individual 100 m grid cells within the reference polygons[50]. Each sampled grid cell, together with the LCZ label assigned to its reference polygon and its extracted predictor values, constituted one reference sample. Thus, sample counts refer to individual grid cells rather than manually delineated polygons. To limit class imbalance and computational demand, these reference samples were capped at 3,000 per LCZ class for each city and target year. Classes exceeding this limit were reduced by reproducible random subsampling, whereas all samples from smaller classes were retained at this stage. Sample counts after capping, before training–validation partitioning and subsequent filtering, are reported in Supplementary Tab 2, and their spatial distributions are shown in Supplementary Figs. 16 and 17.

The predictor stack combined spectral and textural information with indicators of built form, human activity, vegetation and terrain. Harmonized Landsat and Sentinel-2 surface reflectance (HLS)[51] provided six bands: blue, green, red, near-infrared and two shortwave-infrared bands. The Landsat-based L30 product was used for the nominal 2013 maps and the Sentinel-2-based S30 product for 2024. March–June selection windows were used in both target years.

Scenes with cloud-cover metadata values below 30% were selected, and pixels flagged as cloud, cloud shadow or snow/ice were excluded using Fmask[52] before median compositing. Remaining gaps were filled from median composites of scenes with cloud cover below 5%, without additional pixel-level Fmask screening of this fallback composite. For each of the six spectral predictors, local mean and standard deviation were calculated using a circular image window with a radius of one pixel. Contrast and homogeneity (inverse difference moment) were derived from gray-level co-occurrence matrices (GLCMs) within a 3 × 3-pixel square image window. These matrices summarize the co-occurrence of pairs of pixel values[53]. The texture metrics were averaged across the four default directional orientations: horizontal, vertical and the two diagonals.

Annual nighttime-light conditions were represented by the median radiance of monthly VIIRS Day/Night Band composites[54]. Four GHSL predictors described total and non-residential built-up surface area and built volume[55]. Values for 2013 were linearly interpolated between the 2010 and 2015 layers, and values for 2024 between the 2020 and 2025 layers. Additional predictors comprised LandScan population[56], canopy height[57], bare surface frequency[58], probabilities of cultivated and natural or semi-natural grassland[59], and FABDEM elevation[60]. Population and grassland layers from 2013 were used for the 2013 stack, whereas the 2024 stack used population data from 2023 and grassland probabilities from 2022. Canopy height, bare-surface frequency and elevation were used as static covariates for both target years. The resulting stack contained 41 predictors per target year (Supplementary Tab 3).

Classification and validation

Separate Random Forest classifiers were trained for each city and target year in Google Earth Engine, using 500 trees, a fixed random seed and otherwise default parameters[61]. A hybrid validation design combined spatial separation for common classes with within-class splitting for rare classes. Classes containing at least 500 reference samples after capping were evaluated using buffered spatial-block validation. Each city was divided into 2 km × 2 km blocks, which were assigned to five folds using a fixed random seed. One fold was held out for validation and four were used for training. Training samples within 500 m of the validation blocks were excluded. This was a single spatial holdout, rather than repeated five-fold cross-validation.

Classes with fewer than 500 samples were split into approximately equal training and validation subsets, retaining at least one sample in each subset where possible. Classes represented by a single sample were used for training only. Rare-class validation samples within 100 m of the final training set were removed to reduce local spatial overlap. The training and validation datasets combined the respective subsets from the common and rare classes. Classification accuracy was evaluated against the held-out samples, with overall accuracy expressing the proportion assigned to the correct LCZ class. This hybrid

design retained rare classes in the assessment while reducing spatial dependence among the more abundant samples.

The trained classifiers were applied to the annual predictor stacks to generate 100 m LCZ maps. A 3 × 3 majority filter reduced isolated classification noise[62]. The maps were subsequently aggregated by majority voting to the nominal 375 m grid (e.g., VIIRS LST scale) used for trajectory mapping and thermal analysis. Subsequent analyses were restricted to the 5 km-buffered study footprints.

Mapping urban growth trajectories

Urban growth trajectories were identified from pixel-wise LCZ transitions between 2013 and 2024. *Urban expansion* comprised transitions from natural LCZ classes A–G to urban classes 1–10, capturing the conversion of vegetation, bare surfaces or water to urban land. *Urban densification* comprised transitions between urban LCZ classes that represented increasing development intensity through horizontal infill, vertical intensification, or both. Horizontal infill included transitions from open or sparsely built forms to more compact forms, whereas vertical intensification included transitions from low- or mid-rise to higher-rise classes. The classification followed the transition framework in Fig. 1.

Pixels assigned to the same urban LCZ class in both years were classified as *unchanged urban LCZ*. This category denotes stability of the mapped LCZ class but can include physical changes that remain within class boundaries. Subsequent trajectory comparisons used pixels assigned to urban expansion, urban densification or unchanged urban LCZ; other pixels were excluded from those comparisons.

Radial characterization of urban growth

To compare the spatial organization of growth among cities of different sizes, distance from a common city center was normalized by a city-specific maximum radius. For each city, the center was defined as the centroid of its merged 5-km-buffered GHUB boundary geometry. The maximum radius, X, was defined as the greatest distance from that centroid to a vertex of the resulting boundary. For the growth analysis, grid-cell centers

were assigned to successive 1-km annuli within the circle of radius X, with the outermost annulus truncated at X. The analysis used the portion of this circle covered by the trajectory raster grid. For growth category k (expansion, densification or unchanged urban LCZ) and annulus j, the area share was calculated as

$$P_{k,j} = 100 \times \frac{n_{k,j}}{N_j} \quad (1)$$

where $n_{k,j}$ is the number of grid cells assigned to growth category k and N_j is the total number of grid cells in that annulus within the circular raster domain. Raw shares were calculated for annuli containing at least 20 grid cells. For display, profiles were smoothed with a centered three-annulus moving average of the available finite shares. Annular midpoint distances, including the midpoint of the truncated outermost annulus, were divided by X to obtain normalized radial positions. Total areas were calculated separately for each trajectory category using pixel counts on the original 375 m trajectory grid.

SUHI intensity calculation

Daytime and nighttime LST were obtained from the daily VIIRS 375 m product[30], with approximate overpass times of 13:30 and 01:30 local time, respectively. The analysis covered the March–June warm seasons of 2013–2024. Observations were screened for cloud coverage below 10% and view zenith angles of 40° or less, and cloudy pixels were excluded. For each pixel and year, warm-season LST was calculated as the arithmetic mean of retained daily observations, separately for daytime and nighttime.

SUHI intensity was defined relative to a temporally consistent natural reference within each city's study region. Reference pixels were required to retain the same natural LCZ class in 2013 and 2024. Eligible classes were LCZ A–F; water (LCZ G) was excluded.

Pixel-level SUHI intensity was then calculated as

$$SUHI_{i,c,t,d} = LST_{i,c,t,d} - B_{c,t,d} \quad (2)$$

where i denotes a pixel, c a city, t a year, d the daytime or nighttime observation period, and B the corresponding mean natural-reference LST. Annual SUHI fields thus

represented the contrast between local seasonal LST and the same city's natural background. Their temporal changes reflect temperature changes in both the focal pixels and the reference; a positive SUHI trend does not by itself establish increasing absolute LST.

To assess sensitivity to the natural-reference definition, we recalculated SUHI intensity using the mean LST of pixels classified as LCZ D (low plants) in both 2013 and 2024 within each city's study region. Daytime and nighttime trends were then re-estimated using the same approach described below. Trajectory-specific trend distributions and densification–expansion differences were compared with those obtained using the primary LCZ A–F reference (Supplementary Fig. 10).

Temporal trends of SUHI intensity

Long-term SUHI intensity trends were estimated separately for each city and observation period using the annual 2013–2024 SUHI intensity. Temporal dependence was accommodated using pixel-wise linear regression with first-order autoregressive [AR(1)] errors, implemented with the fitAR_map function in remotePARTS[63]. For each pixel, the model was

$$SUHI_{i,t} = \alpha_i + \beta_i t + u_{i,t} \quad (3)$$

$$u_{i,t} = \phi_i u_{i,t-1} + \varepsilon_{i,t} \quad (4)$$

where α_i is the intercept, β_i is the annual trend, $u_{i,t}$ is the temporally correlated error, ϕ_i is the first-order autoregressive coefficient, and $\varepsilon_{i,t}$ represents a new random error at pixel i in year t and is assumed to be independent across years. The autoregressive parameter was estimated by restricted maximum likelihood. With annual observations ordered chronologically, the default unit-spaced time index represents successive years. The coefficient of time was extracted as the trend in K year^{-1} and multiplied by ten for reporting in K decade^{-1}. Only pixels belonging to the three urban growth trajectories and having a valid trend estimate were retained; valid zero trends were included.

Comparisons among urban growth trajectories

To assess associations between urban growth and SUHI change, pixel-level trend distributions were summarized separately for expansion, densification and unchanged urban LCZ in each city for day and night. We then calculated the city-specific difference between the median trend in densifying areas and the median trend in expanding areas. Positive values indicate higher SUHI trends in densifying areas. To estimate uncertainty while accounting for spatial clustering, we used a spatial block bootstrap with 10,000 replicates. Spatial blocks were resampled with replacement separately within each growth category, retaining their constituent pixels, and the difference between the two median trends was recalculated for each replicate. Block sizes were informed by trajectory-adjusted residual semivariograms and were shared by daytime and nighttime within each city. The city-specific differences were combined using a random-effects meta-analysis. Between-city variance was estimated by restricted maximum likelihood, and pooled 95% confidence intervals were obtained using Hartung–Knapp inference.

To examine whether the difference between densifying and expanding areas persisted at comparable distances from the city center, median SUHI trends in densification and expansion pixels were compared within the same normalized radial zones. These comparisons used the boundary-derived center and maximum radius defined above and were conducted separately for each city and observation period.

To distinguish changes in the urban–natural temperature contrast from changes in absolute surface temperature, we also examined LST trends in expansion, densification, unchanged urban LCZ and natural reference areas, separately for daytime and nighttime. This comparison distinguished SUHI intensification accompanying absolute warming from intensification accompanying a smaller LST decline than in the reference. Decreasing SUHI was likewise interpreted in relation to temperature changes in both the focal and reference areas.

We further examined individual LCZ transitions to identify which pathways contributed to the broader trajectory patterns. Within each city, pathways accounting for at least 10%

of pixels in their respective expansion or densification category were selected for comparison. Their daytime and nighttime trend distributions were examined separately, allowing differences associated with the initial natural cover or the type of urban-form transition to be distinguished within each trajectory.

Data availability

The public input datasets used for LCZ mapping and study-region characterization are available from the following sources. Harmonized Landsat and Sentinel-2 surface reflectance data (L30 and S30)[51] are available through NASA's HLS data portal (https://hls.gsfc.nasa.gov/data-access-and-tools/). GHSL built-up surface and built-volume data, including their non-residential components[55], are available from the European Commission Joint Research Centre (https://human-settlement.emergency.copernicus.eu/downloadWizard.php). LandScan population data[56] are available from Oak Ridge National Laboratory (https://landscan.ornl.gov/). Canopy height data from Meta and the World Resources Institute[57] are available at https://registry.opendata.aws/dataforgood-fb-forests/. Bare-surface frequency data[58] are accessible through the authors' Google Earth Engine application (https://geocis.users.earthengine.app/view/bare-surfaces). Global Pasture Watch cultivated and natural/semi-natural grassland probability maps[59] are available at https://doi.org/10.5281/zenodo.13890401. FABDEM elevation data and links to earlier releases[60] are available through the University of Bristol data record (https://research-information.bris.ac.uk/en/datasets/fabdem-v1-2/).Global Hierarchical Urban Boundaries (GHUB)[46] are available at https://doi.org/10.5281/zenodo.5168383.

Code availability

The code developed for this study is publicly available on Zenodo at https://zenodo.org/records/20122313.

Acknowledgements

The research described in this article was carried out at the Jet Propulsion Laboratory, California Institute of Technology, Pasadena, CA, USA, under contract with the National Aeronautics and Space Administration. ©2026 California Institute of Technology. Support was provided by the NASA Land Cover Land Use Change (LCLUC) program under grant 80NM0018F0590, and by NASA's ECOSTRESS mission.

Author Contributions

C.Y. designed the research, performed the modeling and data analysis, and led the manuscript writing. G.H., R.B., S.S., Q.D., and A.S. contributed to the discussion of ideas, interpretation of results, and revision of the manuscript. G.H. and A.S. supervised the project and contributed to the research design.

References

1. Seto, K. C., Güneralp, B. & Hutyra, L. R. Global forecasts of urban expansion to 2030 and direct impacts on biodiversity and carbon pools. *Proc. Natl Acad. Sci. USA* **109,** 16083–16088 (2012).
2. United Nations, Department of Economic and Social Affairs, Population Division. *World Urbanization Prospects: The 2018 Revision* (United Nations, New York, 2019).
3. Stewart, I. D. et al. Time evolution of the surface urban heat island. *Earth's Future* **9,** e2021EF002178 (2021).
4. Tuholske, C. et al. Global urban population exposure to extreme heat. *Proc. Natl Acad. Sci. USA* **118,** e2024792118 (2021).
5. Roxon, J., Ulm, F.-J. & Pellenq, R. J.-M. Urban heat island impact on state residential energy cost and CO_2 emissions in the United States. *Urban Clim.* **31,** 100546 (2020).
6. Iungman, T. et al. Cooling cities through urban green infrastructure: a health impact assessment of European cities. *Lancet* **401,** 577–589 (2023).
7. Soltani, A., Dehghani, A. & Azizi, P. Volumetric insights into urban growth analysis: investigating vertical and horizontal patterns. *Sustain. Cities Soc.* **130,** 106589 (2025).
8. Zhao, J., Yu, L., Zhao, L., Fu, H. & Gong, P. Asymmetric influence of urban morphology changes on land surface temperature between daytime and nighttime. *Sustain. Cities Soc.* **124,** 106307 (2025).
9. Banerjee, S. et al. Assessing impact of urban densification on outdoor microclimate and thermal comfort using ENVI-met simulations for Combined Spatial-Climatic Design (CSCD) approach. *Sustain. Cities Soc.* **105,** 105302 (2024).
10. Li, Y., Schubert, S., Kropp, J. P. & Rybski, D. On the influence of density and morphology on the urban heat island intensity. *Nat. Commun.* **11,** 2647 (2020).
11. Zhang, W., Jiao, L., Li, B., Zhang, H. & Liu, Y. Spatial heterogeneity of net thermal effects driven by three-dimensional urban expansion: evidence from Wuhan, China. *Urban Clim.* **68,** 103072 (2026).
12. Lefevre, A., Malet-Damour, B., Bénard, F., Boyer, H. & Rivière, G. Integrating urban heat island analysis for sustainable urban planning: insights from Reunion Island. *Build. Environ.* **278,** 112964 (2025).
13. Liu, S. et al. Urbanization is projected to increase local surface temperature by 2100. *Commun. Earth Environ.* **6,** 988 (2025).

14. Yang, H. et al. Surface urban heat island variations under the 3-decadal urban expansion in China: patterns and driving factors. *Sustain. Cities Soc.* **130,** 106640 (2025).
15. Kim, Y., Yoo, C. & Im, J. Nighttime satellite land surface temperature for urban applications: achievements, challenges, and future prospects. *GISci. Remote Sens.* **62,** 2527990 (2025).
16. Sobstyl, J. M., Emig, T., Abdolhosseini Qomi, M. J., Ulm, F.-J. & Pellenq, R. J.-M. Role of city texture in urban heat islands at nighttime. *Phys. Rev. Lett.* **120,** 108701 (2018).
17. Logan, T. M., Zaitchik, B., Guikema, S. & Nisbet, A. Night and day: the influence and relative importance of urban characteristics on remotely sensed land surface temperature. *Remote Sens. Environ.* **247,** 111861 (2020).
18. Chen, G. et al. Effects of urban geometry on thermal environment in 2D street canyons: a scaled experimental study. *Build. Environ.* **198,** 107916 (2021).
19. Wu, W.-B., Yu, Z.-W., Ma, J. & Zhao, B. Quantifying the influence of 2D and 3D urban morphology on the thermal environment across climatic zones. *Landsc. Urban Plan.* **226,** 104499 (2022).
20. Frolking, S., Mahtta, R., Milliman, T., Esch, T. & Seto, K. C. Global urban structural growth shows a profound shift from spreading out to building up. *Nat. Cities* **1,** 555–566 (2024).
21. Mondal, N. & Anand, P. Influence of urbanization on heat exposure risk across Indian cities. *Sustain. Cities Soc.* **135,** 106960 (2025).
22. Beck, H. E. et al. High-resolution (1 km) Köppen–Geiger maps for 1901–2099 based on constrained CMIP6 projections. *Sci. Data* **10,** 724 (2023).
23. Sethi, S. S. & Vinoj, V. Urbanization and regional climate change-linked warming of Indian cities. *Nat. Cities* **1,** 402–405 (2024).
24. Gao, J. & O'Neill, B. C. Mapping global urban land for the 21st century with data-driven simulations and Shared Socioeconomic Pathways. *Nat. Commun.* **11,** 2302 (2020).
25. McManamay, R. A. et al. Dynamic urban land extensification is projected to lead to imbalances in the global land-carbon equilibrium. *Commun. Earth Environ.* **5,** 70 (2024).
26. Stewart, I. D. & Oke, T. R. Local climate zones for urban temperature studies. *Bull. Am. Meteorol. Soc.* **93,** 1879–1900 (2012).
27. Deng, H., Feng, J., Liu, K., Xiong, Y. & Cao, J. Local climate zone framework: seasonal dynamics of surface urban heat island and its influencing factors in three Chinese urban agglomerations. *GISci. Remote Sens.* **62,** 2490317 (2025).
28. Qi, M. et al. Mapping urban form into local climate zones for the continental US from 1986–2020. *Sci. Data* **11,** 195 (2024).

29. Li, Z. et al. Satellite remote sensing of global land surface temperature: definition, methods, products, and applications. *Rev. Geophys.* **61,** e2022RG000777 (2023).
30. Hulley, G. C., Malakar, N. K., Islam, T. & Freepartner, R. J. NASA's MODIS and VIIRS land surface temperature and emissivity products: a long-term and consistent Earth system data record. *IEEE J. Sel. Top. Appl. Earth Obs. Remote Sens.* **11,** 522–535 (2018).
31. Chakraborty, S. et al. Dominant urban form and its relation to nighttime land surface temperature in the rapidly urbanizing National Capital Region of India. *Urban Clim.* **40,** 101002 (2021).
32. Farid, N., Moazzam, M. F. U., Ahmad, S. R., Coluzzi, R. & Lanfredi, M. Monitoring the impact of rapid urbanization on land surface temperature and assessment of surface urban heat island using Landsat in megacity (Lahore) of Pakistan. *Front. Remote Sens.* **3,** 897397 (2022).
33. He, J. F., Liu, J. Y., Zhuang, D. F., Zhang, W. & Liu, M. L. Assessing the effect of land use/land cover change on the change of urban heat island intensity. *Theor. Appl. Climatol.* **90,** 217–226 (2007).
34. Kedia, S., Bhakare, S. P., Dwivedi, A. K., Islam, S. & Kaginalkar, A. Estimates of change in surface meteorology and urban heat island over northwest India: impact of urbanization. *Urban Clim.* **36,** 100782 (2021).
35. Khan, D., Bano, S. & Khan, N. Spatio-temporal analysis of urbanization effects: unravelling land use and land cover dynamics and their influence on land surface temperature in Aligarh City. *Geol. Ecol. Landsc.* **9,** 1326–1375 (2025).
36. Peng, J. et al. Diversified evolutionary patterns of surface urban heat island in new expansion areas of 31 Chinese cities. *npj Urban Sustain.* **4,** 14 (2024).
37. Dirksen, M., Ronda, R. J., Theeuwes, N. E. & Pagani, G. A. Sky view factor calculations and its application in urban heat island studies. *Urban Clim.* **30,** 100498 (2019).
38. Hang, J. & Chen, G. Experimental study of urban microclimate on scaled street canyons with various aspect ratios. *Urban Clim.* **46,** 101299 (2022).
39. Yang, J. et al. Observing the impact of urban morphology and building geometry on thermal environment by high spatial resolution thermal images. *Urban Clim.* **39,** 100937 (2021).
40. Fitria, R., Kim, D., Baik, J. & Choi, M. Impact of biophysical mechanisms on urban heat island associated with climate variation and urban morphology. *Sci. Rep.* **9,** 19503 (2019).

41. Lopez-Cabeza, V. P., Alzate-Gaviria, S., Diz-Mellado, E., Rivera-Gomez, C. & Galan-Marin, C. Albedo influence on the microclimate and thermal comfort of courtyards under Mediterranean hot summer climate conditions. *Sustain. Cities Soc.* **81,** 103872 (2022).
42. Shastri, H., Barik, B., Ghosh, S., Venkataraman, C. & Sadavarte, P. Flip flop of day-night and summer-winter surface urban heat island intensity in India. *Sci. Rep.* **7,** 40178 (2017).
43. Tam, B. Y., Gough, W. A. & Mohsin, T. The impact of urbanization and the urban heat island effect on day to day temperature variation. *Urban Clim.* **12,** 1–10 (2015).
44. Manoli, G. et al. Magnitude of urban heat islands largely explained by climate and population. *Nature* **573,** 55–60 (2019).
45. India Meteorological Department. *Climatological Tables of Observatories in India, 1991–2020* (Climate Research and Services, India Meteorological Department, Pune, 2022).
46. Xu, Z. et al. Mapping hierarchical urban boundaries for global urban settlements. *Int. J. Appl. Earth Obs. Geoinf.* **103,** 102480 (2021).
47. Xian, G. et al. The effects of urban land cover dynamics on urban heat island intensity and temporal trends. *GISci. Remote Sens.* **58,** 501–515 (2021).
48. Massaro, E. et al. Spatially-optimized urban greening for reduction of population exposure to land surface temperature extremes. *Nat. Commun.* **14,** 2903 (2023).
49. Bechtel, B. et al. Generating WUDAPT Level 0 data – current status of production and evaluation. *Urban Clim.* **27,** 24–45 (2019).
50. Bechtel, B. et al. Mapping local climate zones for a worldwide database of the form and function of cities. *ISPRS Int. J. Geo-Inf.* **4,** 199–219 (2015).
51. Claverie, M. et al. The Harmonized Landsat and Sentinel-2 surface reflectance data set. *Remote Sens. Environ.* **219,** 145–161 (2018).
52. Zhu, Z., Wang, S. & Woodcock, C. E. Improvement and expansion of the Fmask algorithm: cloud, cloud shadow, and snow detection for Landsats 4–7, 8, and Sentinel 2 images. *Remote Sens. Environ.* **159,** 269–277 (2015).
53. Honeycutt, C. E. & Plotnick, R. Image analysis techniques and gray-level co-occurrence matrices (GLCM) for calculating bioturbation indices and characterizing biogenic sedimentary structures. *Comput. Geosci.* **34,** 1461–1472 (2008).
54. Elvidge, C. D., Zhizhin, M., Ghosh, T., Hsu, F.-C. & Taneja, J. Annual time series of global VIIRS nighttime lights derived from monthly averages: 2012 to 2019. *Remote Sens.* **13,** 922 (2021).

55. Pesaresi, M. et al. Advances on the Global Human Settlement Layer by joint assessment of Earth observation and population survey data. *Int. J. Digit. Earth* **17,** 2390454 (2024).
56. Dobson, J. E., Bright, E. A., Coleman, P. R., Durfee, R. C. & Worley, B. A. LandScan: a global population database for estimating populations at risk. *Photogramm. Eng. Remote Sens.* **66,** 849–857 (2000).
57. Tolan, J. et al. Very high resolution canopy height maps from RGB imagery using self-supervised vision transformer and convolutional decoder trained on aerial lidar. *Remote Sens. Environ.* **300,** 113888 (2024).
58. Demattê, J. A. M. et al. Bare Earth's surface spectra as a proxy for soil resource monitoring. *Sci. Rep.* **10,** 4461 (2020).
59. Parente, L. et al. Annual 30-m maps of global grassland class and extent (2000–2022) based on spatiotemporal machine learning. *Sci. Data* **11,** 1303 (2024).
60. Hawker, L. et al. A 30 m global map of elevation with forests and buildings removed. *Environ. Res. Lett.* **17,** 024016 (2022).
61. Pal, M. Random forest classifier for remote sensing classification. *Int. J. Remote Sens.* **26,** 217–222 (2005).
62. Yoo, C., Zhou, Y. & Weng, Q. Mapping 10-m industrial lands across 1000+ global large cities, 2017–2023. *Sci. Data* **12,** 278 (2025).
63. Ives, A. R. et al. Statistical inference for trends in spatiotemporal data. *Remote Sens. Environ.* **266,** 112678 (2021).

Supplementary Files

This is a list of supplementary files associated with this preprint. Click to download.

- SupplementaryInformation.docx